

Journal of Fluid Mechanics

<http://journals.cambridge.org/FLM>

Additional services for *Journal of Fluid Mechanics*:

Email alerts: [Click here](#)

Subscriptions: [Click here](#)

Commercial reprints: [Click here](#)

Terms of use : [Click here](#)



Impulsively actuated jets from thin liquid films for high-resolution printing applications

Matthew S. Brown, C. Frederik Brasz, Yiannis Ventikos and Craig B. Arnold

Journal of Fluid Mechanics / *FirstView* Article / January 2006, pp 1 - 30

DOI: 10.1017/jfm.2012.337, Published online: 29 August 2012

Link to this article: http://journals.cambridge.org/abstract_S0022112012003370

How to cite this article:

Matthew S. Brown, C. Frederik Brasz, Yiannis Ventikos and Craig B. Arnold Impulsively actuated jets from thin liquid films for high-resolution printing applications. *Journal of Fluid Mechanics*, Available on CJO 2012 doi:10.1017/jfm.2012.337

Request Permissions : [Click here](#)

Impulsively actuated jets from thin liquid films for high-resolution printing applications

Matthew S. Brown¹†, C. Frederik Brasz¹, Yiannis Ventikos²
and Craig B. Arnold¹

¹ Department of Mechanical and Aerospace Engineering, Princeton University, Princeton, NJ 08544, USA

² Department of Engineering Science, University of Oxford, Parks Road, Oxford OX1 3PJ, UK

(Received 5 September 2011; revised 18 June 2012; accepted 28 June 2012)

Blister-actuated laser-induced forward transfer (BA-LIFT) is a versatile printing technique in which fine jets of ink are ejected from a thin donor film onto an acceptor substrate, enabling high-resolution patterns to be formed. Fluid ejections are initiated by the rapid expansion of micrometre-sized blisters that form on a polymer film underneath the ink layer. Recent work has demonstrated that these ejections exhibit novel flow phenomena due to the unique dimensions and geometry of the BA-LIFT configuration. In this work, we study the dynamics of BA-LIFT printing using a computational model in which fluid is forced by a boundary that deforms according to experimental time-resolved measurements of an expanding blister profile. This allows the model's predictions to be unambiguously correlated with experimental blister-actuated ejections without any fitting parameters. First, we validate the model's predictive capabilities against experimental results, including the ability to accurately reproduce the size, shape and temporal evolution of the jet as well as the total volume of ink released. The validated model is then used to interrogate the flow dynamics in order to better understand the mechanisms for fluid ejection. Finally, parametric studies are conducted to investigate the influence of ink density, surface tension, viscosity and film thickness as well as the size of the blister used. These results provide key insights into avenues for optimization and better control of the BA-LIFT process for improved resolution and repeatability of the printed features.

Key words: breakup/coalescence, jets, thin films

1. Introduction

Laser-induced forward transfer (LIFT) is a versatile direct-write technique, which can print high-resolution ($<5\ \mu\text{m}$, $<1\ \text{fl}$) patterns with a wide range of structural and functional materials (Kyrkis *et al.* 2006; Piqué, Kim & Arnold 2006). Although there are a number of different variations of the LIFT process (Arnold, Serra & Piqué 2007), the general methodology involves focusing a pulsed laser into a thin film of donor material, through a laser-transparent support substrate, resulting in the localized transfer of material onto an acceptor substrate held at a distance. Initially developed to transfer from solid metallic films (Bohandy, Kim & Adrian 1986), LIFT has since been demonstrated with a wide range of fluid materials, from pure liquids to complex

† Email address for correspondence: matthew.sc.brown@gmail.com

reological, multiphase and multicomponent pastes or gels (Piqué *et al.* 1999, 2000; Kyrkis *et al.* 2006; Piqué *et al.* 2006; Arnold *et al.* 2007). In these cases, LIFT has similar functionality to droplet-on-demand inkjet printing in its ability to deposit micrometre-sized droplets of ink into user-defined patterns. However, because LIFT is a nozzleless technique, it can handle a wider range of ink properties and does not suffer from clogging and material compatibility issues associated with the more prevalent nozzle-based techniques.

LIFT is compatible with many complex ink systems that are difficult to pattern using more traditional printing techniques, such as electrochemical energy storage materials for integrated power systems (Arnold *et al.* 2003; Arnold, Kim & Piqué 2004; Wartena *et al.* 2004; Kim, Auyeung & Piqué 2007), sensitive organic and biological solutions for integrated sensors (Serra *et al.* 2004; Colina *et al.* 2005; Boutopoulos *et al.* 2008; Kattamis *et al.* 2009) and even living cells for tissue engineering applications (Barron *et al.* 2004; Hopp *et al.* 2004, 2005; Doraiswamy *et al.* 2006; Kattamis *et al.* 2007). However, despite being validated as a viable means to print these important material systems, the fundamental mechanisms for LIFT are still not fully understood.

Much analytical work has been done to study slender jets using a one-dimensional approximation of the Navier–Stokes equations, yielding similarity solutions that describe how jets approach pinch-off to form droplets (Eggers & Dupont 1994; Eggers & Villermaux 2008). These results apply neatly to inkjet printing (Wijshoff 2008; van Hoeve *et al.* 2010), where the nozzle fixes the initial jet diameter. However, the underlying assumption of quasi-one-dimensional flow breaks down in the case of LIFT, in which the jet draws from the surrounding thin film.

Efforts to characterize the LIFT process have mostly focused on post-transfer analysis of the deposited droplet size and morphology as a function of laser conditions, ink properties and system dimensions (Colina *et al.* 2006; Serra *et al.* 2006; Duocastella *et al.* 2007; Kattamis *et al.* 2007; Boutopoulos *et al.* 2008; Dinca *et al.* 2008; Lin, Huang & Chrisey 2009). These studies show that for a given donor film and incident laser spot size, a minimum volume of ink is transferred at a threshold laser energy. Beyond this threshold, the deposited volume increases with laser energy until the ejections become unstable and the material is no longer deposited within a single compact droplet. To date, this observed deposition behaviour has not been fully correlated to a fundamental understanding of the ejection process.

Time-resolved imaging has been a crucial component in uncovering the nature of the laser-induced transfer mechanisms and identifying the complex hydrodynamic phenomena responsible for the overall deposition behaviour. For example, thermally induced ejection mechanisms, in which the focused laser acts as a point source of heat to the ink, have been shown to result in three distinct regimes of fluid response depending on the incident laser energy (Young *et al.* 2002; Lewis *et al.* 2006; Duocastella *et al.* 2009). At low energies, a bubble of vapourized ink displaces the free surface but subsequently collapses without releasing any material. At high energies, the vapour bubble bursts, ejecting a divergent plume of ink. However, within an intermediate energy range, the ejected material is confined to a narrow jet.

Similar jetting behaviour has also been observed in transfers using an intermediary polymer film, which converts the laser energy into a mechanical impulse delivered to the ink (Brown, Kattamis & Arnold 2010; Kattamis, Brown & Arnold 2011). The thin polymer layer is deposited on a transparent support, typically a glass substrate, before the ink is coated. The laser is absorbed within the polymer film (figure 1*a*), producing a high-pressure gas pocket of ablated material. This forces the remaining solid polymer

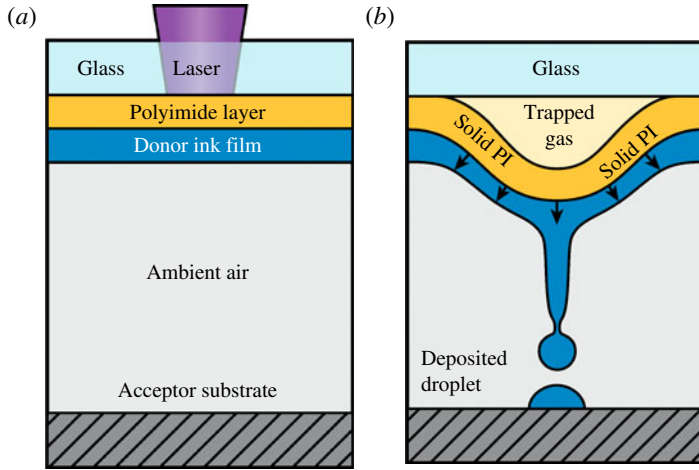


FIGURE 1. (Colour online) Laser-induced forward transfer utilizing a polymer laser-absorbing layer: (a) the laser is absorbed within a thin layer of the polymer film, (b) ablating a confined pocket of gas and forcing the remaining film away from the glass as a rapidly expanding blister. If the impulse provided by the blister is sufficient, a small volume of ink is ejected onto an acceptor substrate.

away from the glass as a rapidly expanding blister. The low thermal diffusivity of the polymer minimizes the thermal interaction with the adjacent liquid (Brown *et al.* 2010; Kattamis *et al.* 2011), and time-resolved images show no evidence of cavitation within the ink film (Brown, Kattamis & Arnold 2011). Therefore, fluid forcing is entirely derived from the expanding blister boundary. The size of the blister produced and the magnitude of the impulse provided to the ink increase with the incident laser energy. Above a threshold energy, this impulse is sufficient to eject a jet of fluid from the ink film (figure 1b), in a process called blister-actuated laser-induced forward transfer (BA-LIFT) (Brown *et al.* 2010; Kattamis *et al.* 2011). At high laser energies, larger and more-disorganized jets are ejected, which may result in complex splashing patterns on the acceptor substrate.

The low-energy jetting regime is generally the most desirable for LIFT printing as it results in the deposition of small, well-defined droplets. Transfer is achieved through the formation of a long, uniform jet that draws from the donor film and achieves a high aspect ratio before pinching off (Duocastella *et al.* 2009; Brown *et al.* 2010, 2011). This detached column of fluid may further fragment into droplets due to the emergence of a Rayleigh–Plateau instability (Plateau 1873; Rayleigh 1878; Eggers 1997). However, these droplets then impact on the acceptor substrate and recombine into a single sessile droplet. Understanding the factors influencing the pinch-off process could motivate ways to better control the volumes of deposited material.

Most quantitative analyses of impulsively driven jets have considered their formation from the free surface of a semi-infinite fluid domain (Blake & Gibson 1987; Zeff *et al.* 2000; Duchemin *et al.* 2002; Antkowiak *et al.* 2007; Tjan & Phillips 2007; Gekle *et al.* 2009). However, the LIFT configuration is unique in that the jet draws from a thin film, in which viscous forces become relevant early in the jetting process (Brown *et al.* 2011). A standard non-dimensional parameter used to characterize the importance of

viscosity in free-surface flows is the Ohnesorge number, $Oh = \mu/\sqrt{\rho\gamma l}$, where μ is the ink viscosity, ρ is the ink density, γ is the surface tension and l is the jet diameter. For small Ohnesorge numbers, viscosity can be neglected when compared to surface tension and inertia. In jets with larger Ohnesorge numbers (e.g. $Oh = 0.5$ in figure 13 of Eggers & Villermaux 2008), long, thin threads form between droplets before breakup.

In addition, due to the small dimensions of the jets produced (5–10 μm in diameter), surface tension has a strong influence on the overall jetting and pinch-off behaviour. This influence can be illustrated by the Weber number $\rho v^2 l / \gamma$, in which v is the jet velocity. Large Weber numbers (>1000) can occur during the initial stages of jetting, in which inertial forces dominate. However, the Weber number rapidly decays as the jet velocity slows and surface tension begins to dominate. Further study into the role of ink properties on the interplay of inertial, viscous and surface forces within this unique regime of thin-film micro-jetting is crucial to the further development of LIFT. By engineering inks with the most appropriate fluid properties, it may be possible to improve printing resolution and repeatability.

In this work, we develop a model of the laser-induced printing process in order to investigate the influence of system parameters on jet formation, pinch-off and the volume of the transferred droplets. The model is based on the blister-actuated transfer mechanism, in which the ink is ejected by a rapidly expanding blister that forms on an intermediary polymer film (figure 1*a,b*). The blister-actuated mechanism offers a number of practical advantages over thermally induced ejection mechanisms (Brown *et al.* 2011). However, it also provides a much simpler framework in which to study ink ejection dynamics because all of the complexities of the laser–material interaction and associated thermodynamic processes are isolated from the fluid by a well-defined, solid boundary, which forces the fluid as it deforms.

The time-resolved blister deformation is experimentally measured and then used as a time-dependent deformable boundary condition in a computational model of the resulting ink ejection. In previous work, we showed that the size and shape of the blisters that form are independent of the presence of an ink layer (Brown *et al.* 2010). This indicates that the fluid–structure coupling does not influence strongly, if at all, the blister’s expansion. Therefore, time-resolved measurements of blisters formed without an ink layer are used to define the time-dependent boundary deformation during the simulated ejections of ink. Experimental measurements are acquired for blisters formed using a range of incident laser energies in order to incorporate the influence of laser energy within the simulations.

The governing equations, assumptions and numerical methods employed in the computational model are described in detail in §3. In §4, we show that the computational results capture trends in a consistent manner that is independent of numerical parameters, such as the grid resolution, once certain refinement thresholds have been reached. Moreover, we validate the physical accuracy of the model by presenting a qualitative and quantitative comparison of simulation results with experimentally captured jet/droplet formations, demonstrating their close agreement. In §5, we use the model to conduct a detailed investigation of the blister-actuated flow dynamics and resulting ejection regimes in order to study the general features of the printing process. Finally, in §6, we use the model’s predictive capabilities to investigate the influence of ink density, viscosity, surface tension, blister size and ink film thickness, among other parameters, on the ejection process.

2. Experimental methods

2.1. Time-resolved blister displacement measurements

Time-resolved blister deformation is measured using an experimental apparatus and procedure detailed in previous work (Brown *et al.* 2010). Blister formation on a 7 μm film of polyimide, coated on a glass slide, is initiated by focusing a 20 ns pulse from a UV laser (Coherent AVIA) into the film to a 20 μm top-hat spot. After a programmable delay, a time-resolved image of the blister is acquired from the side with a microscope (InfiniTube with a Mitutoyo 50 \times Long-WD Objective) and camera (SPOT Insight IN1820) by strobing a 25 ns plasma-discharge lamp (HSPS Nanolite). The image is processed with a custom MATLAB program to extract the blister's outer profile. The entire process is repeated with successive delay times to capture the full temporal progression of the expanding blister. We have previously verified that the blister expansions are highly repeatable and that this imaging technique reproduces the prevailing dynamics in a very satisfactory manner (Brown *et al.* 2010). Time-resolved profile measurements are acquired for blisters formed over a range of laser energies (4.3–14.9 μJ).

The goal is to use these discrete profile measurements to develop a complete functional representation of the expanding blister boundary that can be easily incorporated into our computational model and is continuously defined in time and laser energy. Therefore, we seek to fit a displacement function of the form $\delta = f(r, t, E)$ to the profile data, in which δ is the displacement at radius r and time t of a blister formed with laser energy E . In order to simplify the fitting process, we assume a separable displacement function

$$\delta = X(r, E) \cdot T(t), \quad (2.1)$$

which is the product of a spatial component $X(r, E)$ and a normalized temporal component $T(t)$. The spatial function $X(r, E)$ represents the final size and shape of the blister as a function of laser energy. The assumption of separability implies that during its expansion, the blister takes on a reduced version of this final profile shape, which is uniformly scaled in height by the value (0–1) of the temporal function $T(t)$.

Inspired by analytical solutions of an inflated blister's shape (Arjun & Wan 2005), the spatial function takes the form

$$X(r, E) = H_0(E) \left(1 - \left(\frac{r}{R_0(E)} \right)^2 \right)^C, \quad (2.2)$$

in which the blister's height $H_0(E)$ and radius $R_0(E)$ are functions of laser energy. Equation (2.2) is motivated by solutions for the limiting cases of an inflated blister dominated by pure stretching ($C = 1$) or pure bending ($C = 2$). This expression is fit to each steady-state (500 ns) blister profile generated within the range of laser energies tested to extract the parameters H_0 , R_0 and C . We find that C has an average value of 1.25 ± 0.185 with no clear correlation with laser energy. Therefore, a constant value of $C = 1.25$ is assumed, and (2.2) is refit to the data for H_0 and R_0 . Figure 2 demonstrates the closeness of these fits (dashed lines) to several experimentally measured profiles (solid lines), while figure 3 shows the resulting fitting parameters H_0 and R_0 plotted against laser energy. Finally, H_0 and R_0 (in μm) are fit to the functions

$$H_0(E) = -0.0093 \cdot E^2 + 2.5708 \cdot E - 9.2618 \quad (2.3)$$

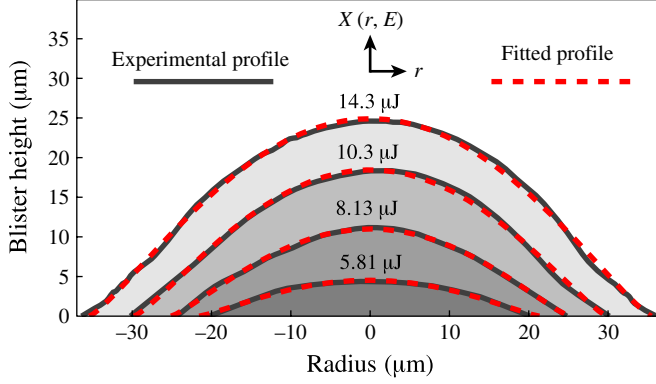


FIGURE 2. (Colour online) Experimentally measured blister profiles (solid lines) shown with their associated fits of (2.2) (dashed lines).

and

$$R_0(E) = 18.117 \cdot \ln(E) - 12.887, \quad (2.4)$$

also shown plotted (solid lines) in figure 3, completing the definition of $X(r, E)$.

The temporal function $T(t)$ represents the evolution of the blister's height normalized by its steady-state value. The data show that for all laser energies, the blisters expand very rapidly for 50–100 ns and reach a constant height within 150–250 ns (Brown *et al.* 2010; Kattamis *et al.* 2011). Therefore, we assume the temporal function is independent of laser energy and attempt to match it to the normalized time response of blisters formed with the highest laser energy (14.9 μJ), which provides the clearest data set for fitting. This data is shown plotted in figure 4. In accordance with the general shape of this dataset, we assume a temporal function of the form

$$T(t) = \frac{2}{\pi} \arctan(t/\tau). \quad (2.5)$$

This expression is fit to the data to extract the time constant $\tau = 2.359 \times 10^{-8}$ s, which is the time for the blister to reach 50 % of its maximum height. Equation (2.5) is also shown plotted in figure 4.

The spatial and temporal evolution of the blister boundary is now fully defined as a function of laser energy input (E). At the threshold for blister formation ($E_{th} = 3.65$ μJ), the blister's diameter is 21.2 μm, which is comparable with the 20 μm laser beam diameter. Beyond threshold, the blister height and radius increase with the laser energy according to (2.3) and (2.4).

2.2. Liquid ejection and deposition

In order to validate the physical accuracy of the computational model, experimental results are also acquired for the blister-actuated transfers of a model ink system, N-methyl-2-pyrrolidone (NMP). NMP is a relevant solvent used in organic ink materials (Kattamis *et al.* 2009). The polyimide film is pretreated with UV light from a mercury lamp to improve its wetting characteristics. NMP is spread on the polyimide surface to a 5 μm film using a Mayer rod, and the completed donor substrate is inverted and suspended 150 μm above a glass acceptor substrate. As

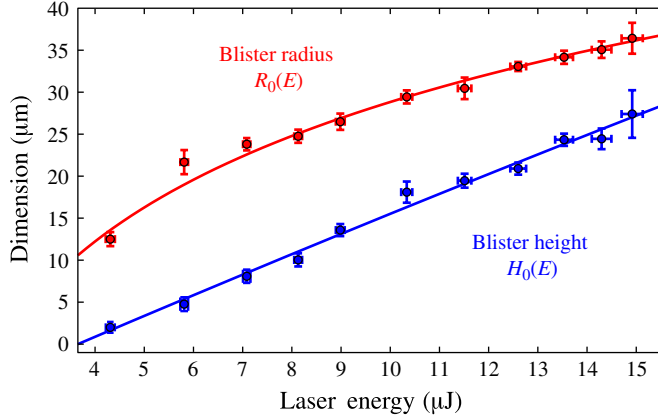


FIGURE 3. (Colour online) The parameters R_0 and H_0 are extracted by fitting (2.5) to blister profiles generated with a range of laser energies. Each data point represents the average of five profile fits, and the vertical error bars indicate ± 1 standard deviation. The horizontal error bars indicate ± 1 standard deviation in the shot-to-shot variation of laser energy. Fits of the extracted blister height (2.3) and width (2.4) versus laser energy are also shown.

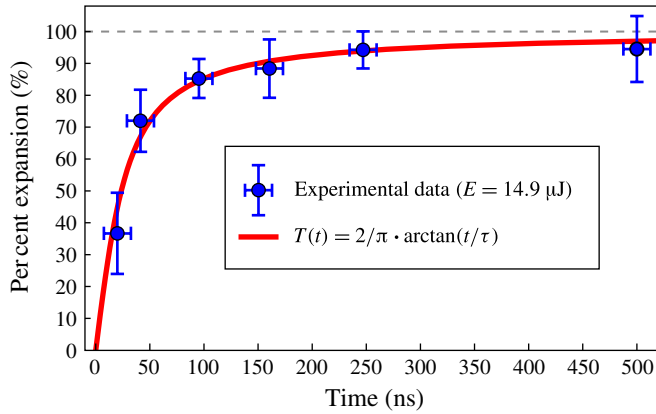


FIGURE 4. (Colour online) (The normalized temporal evolution of blister height initiated with a $14.9 \mu\text{J}$ laser pulse. Each data point represents the average of five measurements, and the vertical error bars indicate ± 1 standard deviation. The horizontal error bars indicate the temporal uncertainty due to the 25 ns exposure time of the images from which the measurements are extracted. A fit to the data (2.4) is also shown, which captures the essential behaviour of the temporal response.

detailed in the previous section, a UV laser pulse initiates the blister expansion, which now results in the ejection of the adjacent liquid. Time-resolved images of the ejected liquid are acquired from the side. The process is repeated for a range of laser energies, producing arrays of printed droplets. The acceptor substrate is removed and imaged from above to extract each droplet's cross-sectional area. From these area measurements, the deposited volume can be estimated by assuming the droplet is a spherical section with a 17° contact angle, a value measured using confocal laser scanning microscopy.

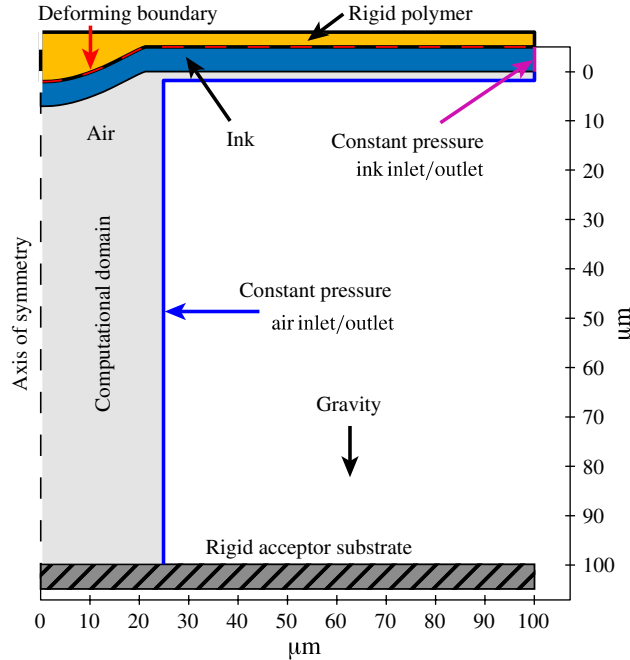


FIGURE 5. (Colour online) Setup of the computational model.

3. Numerical methods

The setup of our computational model is shown in figure 5. The axisymmetric computational domain, which contains both ink and air phases, is bounded on the top and bottom by walls and on the sides by constant pressure boundaries, which allow free inflow/outflow of fluid. A uniform film of ink is suspended from the upper wall, which represents the polymer film surface. This wall is initially flat but then deforms according to (2.1)–(2.5). The deforming boundary imparts momentum to the ink, which begins to flow and displace the ink–air interface. The evolution of this interface as well as the velocity and pressure fields are solved using a multiphysics suite, CFD-ACE+ (ESI Group, Paris, France) (ESI CFD Inc. 2009).

The incompressible mass and momentum conservation equations are discretized on a structured mesh using the finite volume method. The initial mesh is comprised of square cells. However, it is updated each time step in order to accommodate the deforming upper boundary (ESI CFD Inc. 2009). Mesh deformation is accomplished by treating the domain as a linear-elastic solid and solving for the displacements of the interior nodes subject to forcing from the prescribed boundary displacement. This solid-body elasticity analogy ensures the remeshed elements maintain a low aspect ratio with sides that are close to orthogonal.

The ink and air phases are resolved within the domain using the volume-of-fluid (VOF) method (Hirt & Nichols 1981; Rider *et al.* 1995). In this process, a scalar parameter is stored within each grid cell, which represents the volume fraction occupied by ink. The parameter takes on values between 0 (cell filled with air) and 1 (cell filled with ink), with intermediate values indicating that an interface traverses the cell. A second-order, piecewise-linear interface construction (PLIC) is used to determine

fluxes of each phase and calculate the surface tension at the interface (Kothe *et al.* 1996).

The VOF method is a widely used numerical scheme for simulating free-surface flows, and the literature contains numerous examples of computations comparing favourably with experimental and analytical results (Kleefsman *et al.* 2005; Josserand *et al.* 2005; Popinet 2009). Conservation of mass is satisfied intrinsically, and topological changes in the interface are handled naturally without sacrificing fidelity (Kleefsman *et al.* 2005; Popinet 2009), making VOF a viable method for simulating the jet formation and breakup encountered in BA-LIFT.

The conservation equations are marched in time in a fully implicit manner using a Crank–Nicholson method. Together with the use of a central differencing scheme for all spatial derivatives, this combination ensures second-order accuracy in space and time. Time steps are automatically set with a fixed target Courant–Friedrichs–Lewy (CFL) number, which determines the fraction of a cell that a fluid element can traverse within one time step. For this study, we use a CFL number of 0.025, a conservative approach that guarantees little, if any, dependence of the results on the temporal resolution. This constraint results in typical time steps in the range 0.2–2 ns.

Pressure and momentum are coupled using a pressure-correction equation, which is formulated using the SIMPLEC scheme (Van Doormaal & Raithby 1984). The linear systems resulting from the momentum equations are solved in each iteration using a conjugate solver, whereas algebraic multigrid (Webster 1994) is employed for the pressure-correction equations. The equations are iterated in sequence to achieve convergence within each time step.

4. Model validation

In order to verify the plausibility and accuracy of the computational model, we compare experimental and numerical results for the test case of ejections from a 5 μm donor film of NMP ($\mu = 1.7 \text{ mPa s}$, $\rho = 1030 \text{ kg m}^{-3}$, $\gamma = 40.79 \text{ mN m}^{-1}$) into a background of air ($\mu = 18.46 \text{ } \mu\text{Pa s}$, $\rho = 1.1614 \text{ kg m}^{-3}$). We first conduct a detailed discretization analysis to establish an appropriate mesh. This is followed by a detailed comparison of computational results with experimental measurements for transfers initiated with a range of laser energies.

4.1. Discretization analysis

A detailed discretization analysis is conducted to ensure that the simulations capture flow trends in a systematic manner. In order to optimize computational-cell distributions and numbers, we construct multiblock rectangular-grid topologies that exclude regions of the secondary fluid (air) that do not contribute to the overall flow dynamics. This reduces computation time without affecting the salient features of the flow.

The particular computational domain required to capture all relevant flow phenomena is strongly dependent on the specifics of each case simulated. For example, wider and faster jets are produced at high laser energies, which require a broader domain to fully resolve the more vigorous and extended flow in the adjacent air layers. Despite differences in the extent of the domains used, the domains are uniformly populated by square elements. Therefore, a consistent way to present mesh resolution for grid-independence studies is to characterize meshes by the number of elements per micrometre.

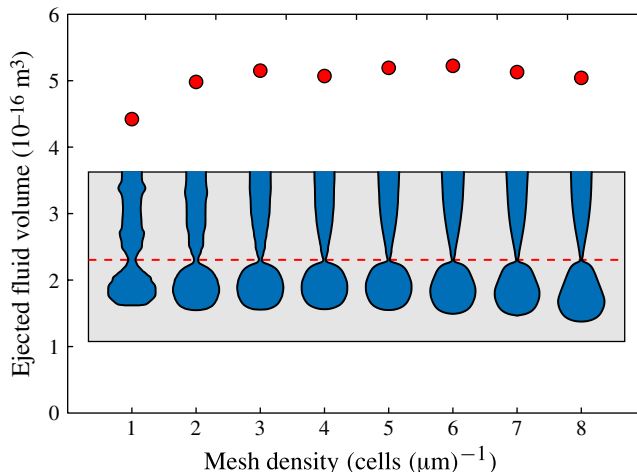


FIGURE 6. (Colour online) Grid-independence study for simulated ejections initiated with $E = 5.27 \mu\text{J}$. Variation in transferred volume is shown plotted as a function of mesh density. Transferred volumes of 0.44, 0.50, 0.52, 0.51, 0.52, 0.52, 0.51 and 0.50 pl correspond to simulations using 1, 2, 3, 4, 5, 6, 7 and 8 cells $(\mu\text{m})^{-1}$, respectively. The inset shows the droplet profiles at the instant of pinch-off for each mesh density. The profiles are shifted vertically to align their pinch-off locations; the distance from the unperturbed ink film surface to the pinch-off location varies by $\sim 17\%$ over the range of grid densities chosen.

To test for grid independence, we compare results using meshes with 1–8 cells $(\mu\text{m})^{-1}$. For each case, we determine the shape of the jet at pinch-off and the volume of ejected fluid (figure 6). As an overall comment regarding this grid-independence study, it is important to note that droplet pinch-off is a singular phenomenon that takes place in exceedingly small spatial extents and temporal durations. As such, it is difficult to pinpoint the exact moment in time when breakup occurs. Nevertheless, we find that with a grid density of 5 cells $(\mu\text{m})^{-1}$ and higher, the shape of the jet/droplet configuration and the transferred volume are resolved in a very satisfactory manner (figure 6). Therefore, we conclude that a resolution of 5 cells $(\mu\text{m})^{-1}$ provides sufficient accuracy for use in our study.

4.2. Comparison of simulation results with experiments

Before utilizing the computational model for conducting parametric studies, we compare sets of simulation results with experimentally measured findings. This comparison involves a qualitative juxtaposition of jet/droplet shapes (shown in figures 7 and 8) as well as a quantitative comparison of ejected ink volumes (figure 9). The latter quantity is chosen because of its fundamental importance in the LIFT process and because it is a convenient metric with which to characterize printing resolution and repeatability during optimization and control studies.

Figure 7 demonstrates the close correlation between the size, shape and temporal evolution of simulated and experimentally produced jets initiated with a $5.4 \mu\text{J}$ laser pulse. This close correspondence is significant considering that no free parameters are utilized to match simulation results with experimental measurements. A similar comparison is presented in figure 8 for jets produced with a higher laser energy ($E = 7.7 \mu\text{J}$). Figure 8(a) shows an experimental image acquired at $8 \mu\text{s}$ of a jet

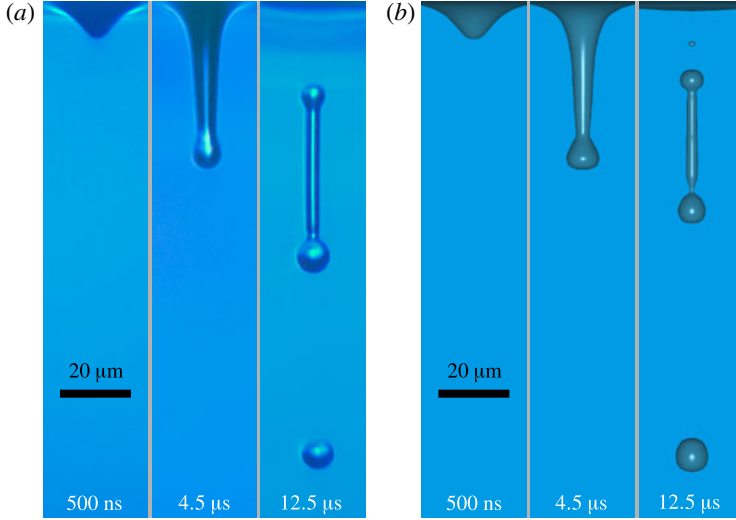


FIGURE 7. (Colour online) (a) Experimentally acquired images and (b) rendered computational results of fluid ejections from a $5\ \mu\text{m}$ donor film of NMP using a $5.4\ \mu\text{J}$ laser pulse. The ejected fluid volume extracted from the last experimental image ($1.2 \times 10^{-15}\ \text{m}^3$) compares favourably with that from the simulated ejection ($1.0 \times 10^{-15}\ \text{m}^3$). Image frames are $134\ \mu\text{m}$ high.

impacting a glass acceptor substrate located $150\ \mu\text{m}$ below the donor substrate. A dynamic contact angle of 45° is observable in the image. These features are accurately reproduced in the corresponding simulated ejection and impact depicted in figure 8(b).

Figure 9 demonstrates the consistency between computational predictions and experimental measurements of transferred ink volume as a function of laser energy. Figure 9 focuses on a smaller range of laser energies near the transfer threshold using a lower-viscosity fluid than is typically studied (Colina *et al.* 2006; Serra *et al.* 2006; Kattamis *et al.* 2007; Boutopoulos *et al.* 2008; Dinca *et al.* 2008; Duocastella *et al.* 2009; Lin *et al.* 2009). A threshold laser energy, below which no fluid is transferred, is experimentally observed at $5.5\ \mu\text{J}$. This value compares favourably with the threshold energy ($5.115\ \mu\text{J}$) predicted by the simulations. In the simulations, a second threshold energy is observed, below which all secondary droplets are reabsorbed by the ink film rather than transferred. This behaviour is further discussed in § 5.2. Beyond threshold, both data sets exhibit a similar dependence on laser energy, with the simulated data points located well within the uncertainty of the experimental measurements. This validates the accuracy of the computational model in resolving the dependence of the ejection process on laser energy input.

5. Dynamics of fluid ejection

In this section, we consider results from simulations initiated using a specific set of simulation parameters in order to assess the general features of the blister-actuated transfer process and its dependence on laser energy input. These results are utilized to develop a fundamental understanding of the ejection process. Then, in subsequent sections, the influence of ink properties and system parameters on the jetting dynamics are elaborated.

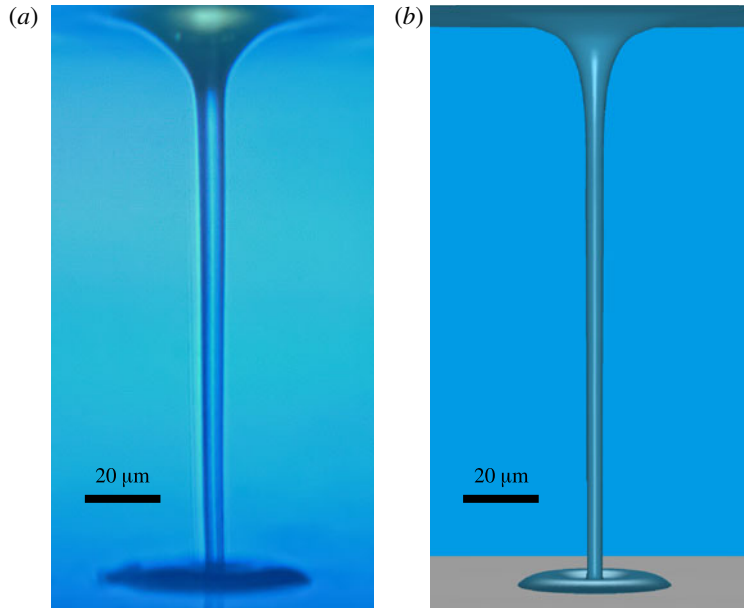


FIGURE 8. (Colour online) (a) Experimentally acquired image of a jet ejected from a $5\ \mu\text{m}$ donor film of NMP acquired $8\ \mu\text{s}$ after a $7.7\ \mu\text{J}$ laser pulse. The jet impacts with an acceptor substrate (glass slide) located $150\ \mu\text{m}$ below the donor substrate. (b) Rendered image of a simulated ejection at $8\ \mu\text{s}$ corresponding to the experimental conditions. A 45° contact angle is imposed at the acceptor–substrate boundary to match the experiment.

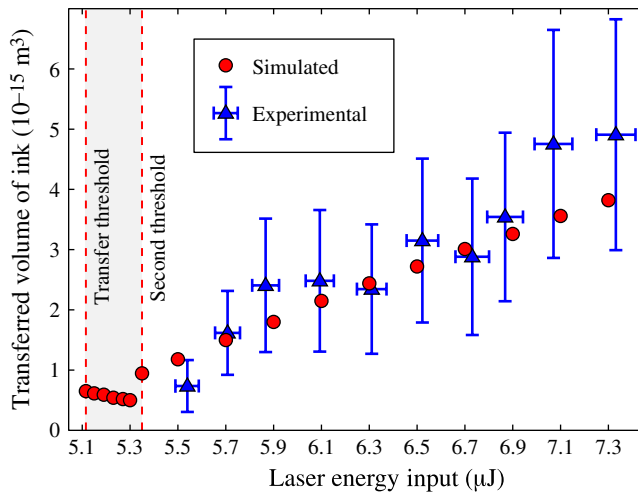


FIGURE 9. (Colour online) Plot of experimentally measured and simulated volumes of ink transferred as a function of laser energy. Each experimental data point represents the average of volumes measured from 10 transferred droplets, and the vertical error bars indicate ± 1 standard deviation. The horizontal error bars indicate ± 1 standard deviation in the shot-to-shot variation of laser energy. The two thresholds are discussed in § 5.2.

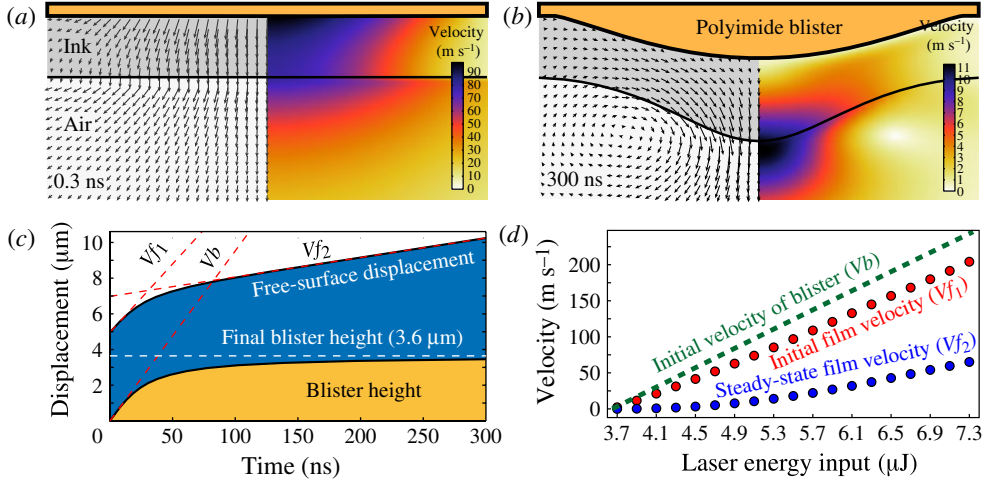


FIGURE 10. (Colour online) Velocity fields at (a) 0.3 ns and (b) 300 ns generated by a rapidly expanding blister formed with $E = 5.115 \mu\text{J}$. (c) Temporal evolution of the free-surface displacement, measured along the axis of symmetry, of the $5 \mu\text{m}$ liquid film relative to the expanding blister’s height ($E = 5.115 \mu\text{J}$). The free surface of the liquid film is initially displaced at a velocity V_{f1} by the blister, which expands at velocity V_b . After the blister expansion has slowed, the free surface continues to propagate with an approximately constant velocity V_{f2} . (d) Scaling of these velocities with the laser energy input. All simulations were conducted assuming the standard ink and air properties.

The standard set of simulation parameters used in this section is representative of an ejection from a $5 \mu\text{m}$ film of NMP ($\mu = 1.7 \text{ mPa s}$, $\rho = 1030 \text{ kg m}^{-3}$, $\gamma = 40.79 \text{ mN m}^{-1}$) into a background of air ($\mu = 18.46 \mu\text{Pa s}$, $\rho = 1.1614 \text{ kg m}^{-3}$). The ejected fluid impacts with an acceptor substrate located $100 \mu\text{m}$ below the donor film. Experimentally acquired images of jet impact with the acceptor substrate, such as figure 8(a), demonstrate an initially large dynamic contact angle, which decays to a lower steady-state value. The evolution of the dynamic contact angle involves a complicated dependence on the contact-line velocity, which is difficult to incorporate within the computational model (Sikalo *et al.* 2005). Therefore, for simplicity, a static 90° contact angle is assumed.

Flow within the donor film can be logically separated and analysed over two different time scales. During early times ($t \lesssim 300 \text{ ns}$), the blister rapidly expands and drives flow within the liquid film. The kinetic energy transferred to the liquid during this early period provides the impetus for its continued downward progression into a free-surface jet after the blister has stopped expanding. The magnitude of this transferred kinetic energy is important in determining the jetting behaviour during later times ($t \gtrsim 300 \text{ ns}$).

5.1. Early time behaviour: blister-actuated flow

Fluid motion is initiated by the large downward velocity imposed at the deforming blister boundary. For example, figure 10(a) shows the initial velocity field developed around an emerging blister formed with a laser energy $E = 5.115 \mu\text{J}$. At this very early time (0.3 ns), the boundary is still approximately flat, but it is rapidly deforming at 98 m s^{-1} at its centre. This propels the contacting layer of fluid near the centreline downward at the same rate since lateral flow is initially very weak. Away from the

centreline, an outward radial velocity component develops as the fluid is displaced away from the blister's centre.

As the blister grows, its expansion rate continuously decreases (figure 4). This causes fluid in direct contact to decelerate due to the no-slip, no-flow-through boundary conditions. However, a high-energy region of fluid begins to migrate from the wall and continues to flow downward, exceeding the wall velocity. Off from centre, the radial velocity component eventually reverses and fluid is pulled into the centre by this high-energy pocket (see supplementary movie 1, available at <http://dx.doi.org/10.1017/jfm.2012.337>). By 300 ns, the blister has expanded to 95 % its final size, and its expansion rate, measured at its centre, has slowed to 0.6 m s^{-1} (figure 10*b*). The region of highest fluid velocity (11 m s^{-1}) has now migrated to the free surface of the liquid film. The temporal evolution of the free-surface displacement relative to the blister height during this initial period is shown in figure 10*c*.

Although figure 10*a–c* shows results for the specific case of $E = 5.115 \text{ }\mu\text{J}$, the same general behaviour is observed for all of the laser energies considered ($E = 3.7\text{--}7.3 \text{ }\mu\text{J}$), with velocities that scale with the laser energy input. The characteristic velocities V_b , V_{f1} and V_{f2} , defined within figure 10*c*, are shown plotted against laser energy input in figure 10*d*. The blister's initial expansion velocity V_b , determined from (2.1)–(2.5), increases approximately linearly with laser energy over this range. As the blister initially expands, it displaces the free surface of the liquid film downward at a rate V_{f1} . However, because liquid is also partially being displaced in the outward radial direction, V_{f1} is only a fraction of V_b . This fraction increases from 66 % at $E = 3.7 \text{ }\mu\text{J}$ to 83 % at $E = 7.3 \text{ }\mu\text{J}$, which can be attributed to a corresponding increase in blister width with laser energy. As the blister width becomes large relative to the liquid film thickness, the radial component of the fluid's initial velocity near the blister's centre decays to zero.

During the blister's expansion, velocities within the liquid film rapidly decrease due to the decelerating blister boundary. As the blister approaches its final dimensions, the liquid's free-surface velocity decays to a relatively steady-state velocity V_{f2} for the remainder of this early time period, decreasing only slightly due to viscous dissipation and surface tension. The dependence of the steady-state velocity (V_{f2}) on laser energy input is shown in figure 10*d*.

The relative importance of viscous and surface forces can be seen in figure 11*a*), which shows the kinetic energy of the flow plotted against time for jets initiated with several different laser energies. The solid lines represent simulation results conducted using the standard ink and air properties, while the dashed lines indicate inviscid simulations without surface tension. Comparison of the two curves at each laser energy shows that during early times ($t \leq 300 \text{ ns}$), relatively little kinetic energy is viscously dissipated or converted into surface energy. The fluid's kinetic energy at 300 ns is also plotted against laser energy input in figure 11*b*). The data is presented on a log–log plot in order to demonstrate a power-law dependence, which exhibits an exponent of 4.5.

One can consider a simple model of the blister expansion and fluid motion in order to rationalize the magnitude of the exponent shown in figure 11*b*). According to (2.2) and (2.5), the expanding blister reaches a height of H_0 and radius of R_0 within a time of order τ , with τ assumed to be independent of laser energy E , as observed experimentally and discussed in §2.1. Therefore, to a rough approximation, the blister motion imparts a velocity $v \sim H_0/\tau$ to a disc of fluid of height H_f and radius R_0 , where H_f is the ink film thickness. The kinetic energy (E_k) of this fluid disc then

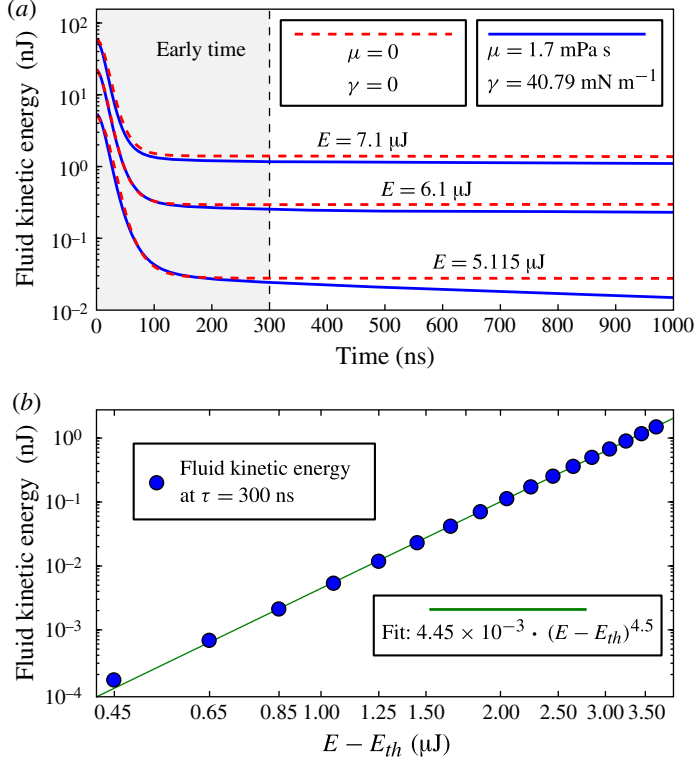


FIGURE 11. (Colour online) (a) Total kinetic energy within the computational domain, including ink and air phases, plotted against time. Solid lines represent simulation results using the standard ink and air properties. Dashed lines indicate simulations without viscosity or surface tension. (b) Kinetic energy at 300 ns plotted against laser energy input (E) minus the threshold laser energy for blister formation ($E_{th} = 3.65 \mu\text{J}$). A log–log plot is used in order to demonstrate the power-law dependence (exponent equals 4.5).

scales as

$$E_k \sim \frac{\rho R_0^2 H_0^2 H_f}{\tau^2}. \quad (5.1)$$

Based on figure 3, we can approximate $H_0(E) \sim E$ and $R_0(E) \sim E$, resulting in $E_k \sim E^4$, which suggests that the power-law exponent of 4.5 is plausible.

Although this simplistic model approximately reproduces the observed power-law scaling, it neglects some key aspects of the process. Treatment of the disc velocity as proportional to H_0/τ may be representative of the initial velocity field of the fluid, and hence the initial kinetic energy. However, it neglects the details of the full temporal evolution of the blister's shape as it slows and pulls kinetic energy back out of the fluid. The free-surface curvature imposed by the blister's shape can have a strong influence on the magnitude of the kinetic energy exchanged with the fluid during the impulsive acceleration and deceleration of the blister boundary (Antkowiak *et al.* 2007). More-advanced analytical models are required to fully capture these effects. However, they fall outside the scope of this paper.

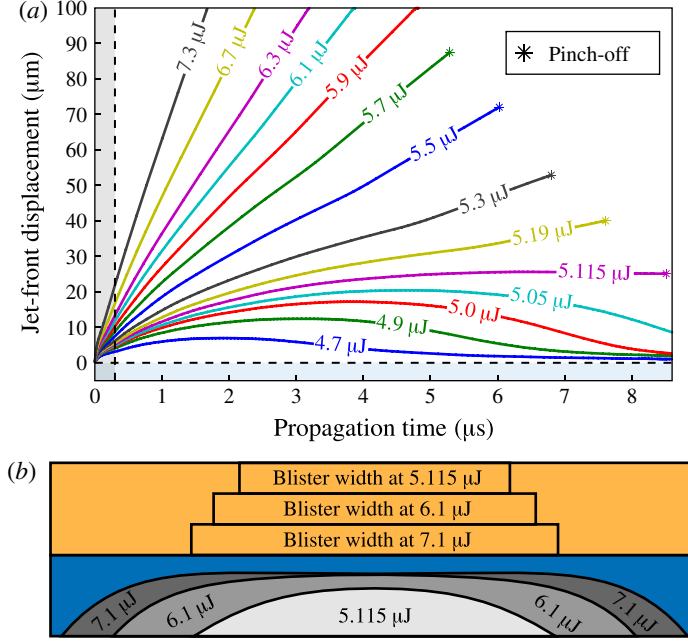


FIGURE 12. (Colour online) (a) Trajectories of jets initiated with a range of laser energies (4.7–7.3 μJ). For laser energies below 5.115 μJ , the jets reach a maximum length and then retract back into the film. At 5.115 μJ and above, liquid pinches off from the jet with a positive velocity in the direction of the acceptor substrate, located 100 μm away. The time and corresponding jet length at the moment of pinch-off is indicated with an asterisk (*). Initial pinch-off occurs earlier and from a longer jet as the laser energy is increased. At 5.9 μJ and above, the jet impacts with the acceptor substrate before pinch-off occurs. (b) An illustration, derived from simulation results, showing the region of the initial ink film from which fluid is ejected for several laser energies (5.115, 6.1 and 7.1 μJ).

5.2. Longer-time behaviour: ejection regimes

The jetting trajectory during later times ($t \gtrsim 300$ ns) is largely determined by the initial laser energy input and the resulting magnitude of kinetic energy transferred to the liquid during the blister's expansion. Results from the previous section show that the early-time flow behaviour ($t \lesssim 300$ ns) is qualitatively consistent for all laser energies considered. However, as the jet continues to advance, it becomes slowed by viscous and surface forces, resulting in jetting dynamics that bifurcate into distinct regimes depending on the available kinetic energy.

Figure 12(a) shows jet-front propagation distance as a function of time for various laser energies. Below 5.1 μJ , the jet's kinetic energy is insufficient for it to escape the pull of surface tension, and it retracts back into the film without detaching a droplet (figure 13a). Between 5.1 and 5.115 μJ , a droplet is detached during the jet's retraction, but its velocity is in the direction of the liquid film. Therefore, it does not result in liquid being transferred to the acceptor substrate. However, at 5.115 μJ , a droplet is released with a small but positive velocity away from the liquid film (figure 13b and supplementary movie 2). This critical event corresponds to the transfer threshold depicted in figure 9. The transfer threshold is determined from the

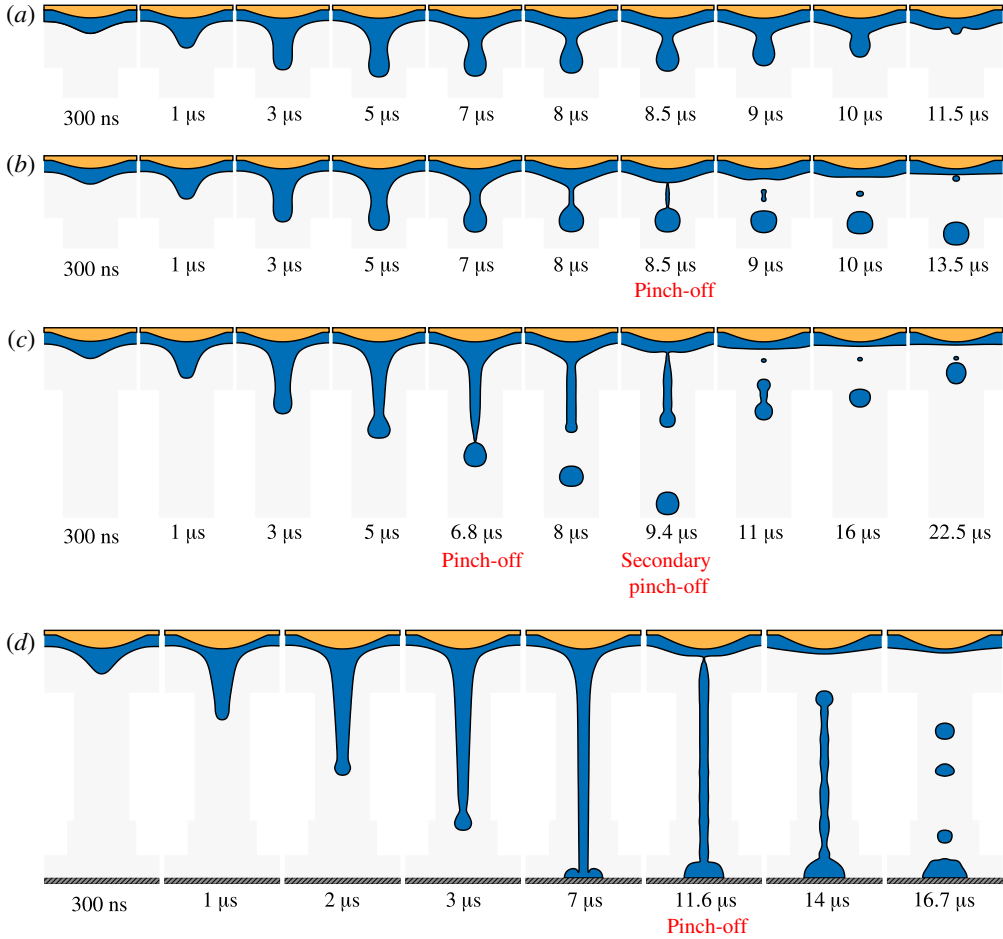


FIGURE 13. (Colour online) Simulation results for blister-actuated flows using standard ink properties initiated with laser energy inputs of: (a) $E = 5.1 \mu\text{J}$ (below threshold); (b) $E = 5.115 \mu\text{J}$ (transfer threshold); (c) $E = 5.3 \mu\text{J}$ (below second threshold); (d) $E = 6.1 \mu\text{J}$ (impact with acceptor).

simulations within 1 nJ by demonstrating that transfer occurs at $E = 5.115 \mu\text{J}$ but not at $E = 5.114 \mu\text{J}$. In addition to the main droplet, a smaller satellite droplet forms. However, this droplet impacts with the donor film and does not contribute to the transferred volume.

Segmentation of the jet into droplets can be attributed to the Rayleigh–Plateau instability (Plateau 1873; Rayleigh 1878; Eggers 1997). A general feature of cylindrical-jet breakup is that the diameters of the droplets produced scale with the jet diameter (Rayleigh 1878; Teng, Kinoshita & Masutani 1995). As laser energy is increased beyond the transfer threshold, the jets become more elongated and narrower at their tip before the onset of the instability. This reduces the size of the initial droplet that forms from the tip. In addition, for a small range of laser energies near the transfer threshold (5.115–5.3 μJ), only the outermost droplet is released with a positive outward velocity (figure 13c). This behaviour results in the initial decrease in transferred volume with increasing laser energy depicted in figure 9. The simulation

results show a 23 % decrease in transferred volume at 5.3 μJ versus that at the transfer threshold (5.115 μJ), resulting in a droplet volume equivalent to a 12.4 μm diameter hemisphere (0.5 pl). This behaviour is not clearly observed within the experimental results of figure 9 because the scale of this reduction is within the uncertainty of the measurements.

Increasing the laser energy further (5.35 μJ), a second threshold is reached, in which additional droplets are ejected with a positive velocity (figure 9). This accounts for the sharp increase in the total transferred volume depicted in figure 9. Beyond this second threshold, the deposited volume increases approximately linearly with laser energy.

For laser energies below 5.9 μJ , the fluid pinches off from the jet before impacting the acceptor substrate. In these cases, the presence of the acceptor substrate has no effect on the pinch-off process other than the weak interaction mediated by the ambient air. At higher laser energies, the jet impacts with the acceptor substrate before pinch-off occurs, allowing forces from the rigid wall to directly influence the jetting dynamics (figure 13*d* and supplementary movie 3 depict transfer at $E = 6.1 \mu\text{J}$). In these cases, pinch-off always proceeds first from the base of the jet.

To gauge the extent of the acceptor substrate's influence on the transfer process, we consider simulated ejections initiated with $E = 6.1 \mu\text{J}$ in which the distance between the donor film and acceptor substrate is varied. We find that for gap distances between 50–150 μm , the transferred volume changes by less than 0.5 %. Similarly, over this range, changing the contact angle at the acceptor substrate between 0–180° alters the transferred volume by less than 0.3 %, indicating a weak influence of the acceptor substrate on the ejection process for relatively large separations. However, decreasing the gap distance to 25 μm results in a 21 % reduction in the transferred volume because the jet becomes slowed by the impact and ultimately pulls less fluid from the donor film. With a gap distance of 10 μm , a semistable liquid bridge forms between the donor and acceptor substrates, which persists for at least the 100 μs simulation time.

Further interrogation of the fluid transport can be achieved by numerically tracking the cumulative displacement of individual fluid elements within the ink film. At the start of each simulation, an array of points is seeded into the fluid domain, representing passive tracer particles. Between each time step, the positions of the particles are updated by integrating the velocity field. The evolution of tracer particles for the case of a threshold transfer ($E = 5.115 \mu\text{J}$) is shown in supplementary movie 4. The particle tracking process also allows us to map fluid elements that end up in ejected droplets back to their original locations within the ink film. Figure 12(*b*) shows the regions of the ink film that are ejected using several laser energies. The figure demonstrates that there is a region of fluid adjacent to the polyimide film that is not released.

5.3. Transfer-threshold regime

Ejections initiated within a narrow range of laser energies above the transfer threshold represent the most relevant regime for high-resolution printing of functional materials because this produces the smallest deposited volumes and minimizes the stresses placed on the ink. Therefore, additional focus on the dynamics of this important threshold regime is warranted in order to give further insight into the factors that control the threshold and determine the fundamental lower limit on transferable volume.

The dynamics of the blister-actuated ejections are governed by an interplay of inertial, viscous and surface forces. The driving force for fluid motion is provided by

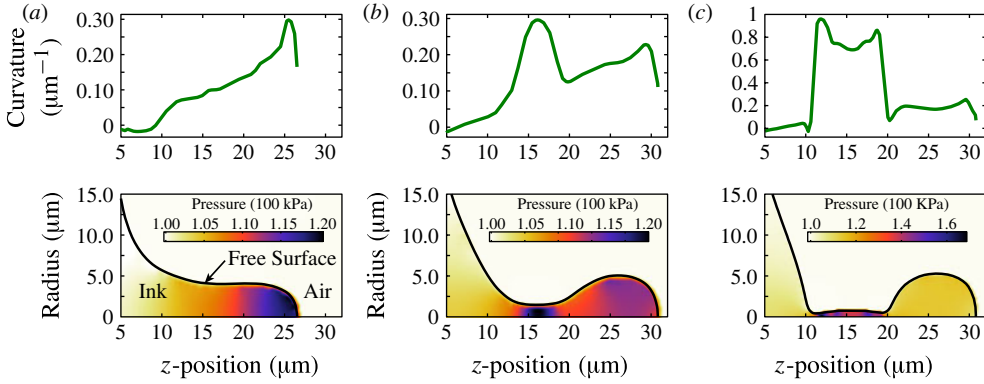


FIGURE 14. (Colour online) Simulated threshold ejection ($E = 5.115 \mu\text{J}$) using standard ink properties. (Bottom) Pressure fields inside the ink at various times: (a) $3 \mu\text{s}$; (b) $7.5 \mu\text{s}$; and (c) $8.3 \mu\text{s}$. A black line indicates the free surface of the ink. At these times, the pressure fields are largely determined by the surface tension, which produces a pressure increase across the interface that is proportional to the mean curvature. (Top) Corresponding plots of mean curvature versus z -position along the jet.

the remnant kinetic energy that persists after the blister's expansion has ceased. This fluid motion is resisted by viscous stresses, which dissipate the kinetic energy as heat. As a jet begins to form at the free surface, surface tension acts to resist the increase in curvature that develops. The local pressure increase (Δp) across the interface can be related to the local mean curvature (κ) and the surface tension (γ) through the Young–Laplace equation

$$\Delta p = \gamma \kappa. \quad (5.2)$$

As large curvatures develop, the pressure field inside the liquid becomes increasingly influenced by surface tension. Figure 14 shows the pressure field at various times during a threshold transfer ($E = 5.115 \mu\text{J}$). The corresponding mean curvature of the free surface is also shown above for each time. Because the free-surface profile shown represents a three-dimensional axisymmetric rotation, the mean curvature has an in-plane and out-of-plane component. At $3 \mu\text{s}$ (figure 14a), the mean curvature increases monotonically along most of the jet axis. This produces a corresponding pressure gradient along the axis, which resists the jet's advance.

The relative influence of surface tension can be characterized by the Weber number, $We = \rho v^2 l / \gamma$, which was introduced in § 1. The Weber number represents the ratio of the fluid's kinetic energy to its surface energy. The threshold for fluid pinch-off corresponds to a transferred kinetic energy that can sufficiently overcome surface tension (i.e. a critical We) to produce a deformation to the free surface that becomes unstable to capillary forces. Although surface tension initially resists the growth of this free-surface protrusion, it is ultimately required for pinch-off to occur. Simulations without surface tension and no acceptor substrate demonstrate that even with arbitrarily small kinetic energies, the jet maintains a tapered shape and continues downward for all times without pinching off. Surface tension is required for the initial broadening of the jet tip into a bulbous shape.

Pinch-off is initiated when a local maximum in curvature develops, producing a local maximum in pressure along the jet axis (figure 14b). This forces fluid in opposite directions on either side of the high-pressure region. As fluid diverges axially from

this region, the local jet radius decreases to maintain continuity, further increasing the curvature and amplifying the process (figure 14c). This argument relies on a quasi-one-dimensional treatment of the pressure field along the axis. Therefore, it does not apply for the local maximum that is visible near the tip of the jet.

Traditional analyses of cylindrical jet breakup predict droplet diameters that are approximately twice the initial jet diameter (Rayleigh 1878; Teng *et al.* 1995). More-recent studies of jet breakup have had great success predicting droplet shapes using a one-dimensional lubrication model (Eggers & Dupont 1994; van Hoeve *et al.* 2010). However, these results are derived assuming long, initially uniform jets, such as those ejected from a nozzle, in which an initial jet diameter is well defined. In the present case of figure 14, the jet is relatively short, and its diameter varies with axial position at all times during its progression. This makes it difficult to define an initial jet diameter. Nevertheless, using the jet midpoint at $3\ \mu\text{s}$ (figure 14a), when the jet diameter is most uniform, as a reference for the initial diameter ($8\ \mu\text{m}$), we find that the ejected droplet diameter ($10.8\ \mu\text{m}$) is only 1.35 times larger. This discrepancy with the ratio of 1.91 for initially uniform jets (Rayleigh 1878) is not surprising given the significant differences in jet shape.

6. Parametric studies

In the following sections, we consider the influence of ink properties and system parameters on the blister-actuated ejection process within the threshold regime. The laser energy required to achieve transfer, the resulting transferred volume, as well as the shape and size of the jet at pinch-off are investigated as a function of ink density, surface tension, viscosity and film thickness as well as the blister size. Within each section, simulation parameters are centred around the standard set used in the previous sections except that a single parameter is systematically varied in order to investigate its influence.

The motivation for these parametric studies is to understand the functional dependencies that are relevant to the technological application of LIFT. In particular, enhancing printing resolution (increasing DPI and reducing line roughness) is a key goal. Because the achievable resolution of a printed feature is highly dependent on the properties of the acceptor substrate (e.g. contact angle and porosity), we choose droplet volume as a more generically relevant parameter. In addition, in all cases studied in this section, the droplets pinch off before hitting a substrate. Therefore, the results are completely independent of acceptor-substrate influence.

For each set of simulation parameters, the transfer threshold is determined by identifying two laser energies between which the simulations exhibit a transition from below-threshold to above-threshold behaviour. Intermediate energies are iteratively tested until the interval bounding this transition is sufficiently small. For example, with the standard set of simulation parameters (see § 5), transfer is observed at $E = 5.115\ \mu\text{J}$ but not at $E = 5.114\ \mu\text{J}$. Therefore, the transfer threshold is determined to be $E = 5.115\ \mu\text{J}$ with 1 nJ of uncertainty.

6.1. Ink density

Because the ink is modelled as an incompressible fluid and its initial forcing is provided through a prescribed boundary displacement, which sets the fluid's velocity along the boundary, the fluid's density has little influence on the velocity field that develops during the blister's expansion. In fact, without viscous and surface tension

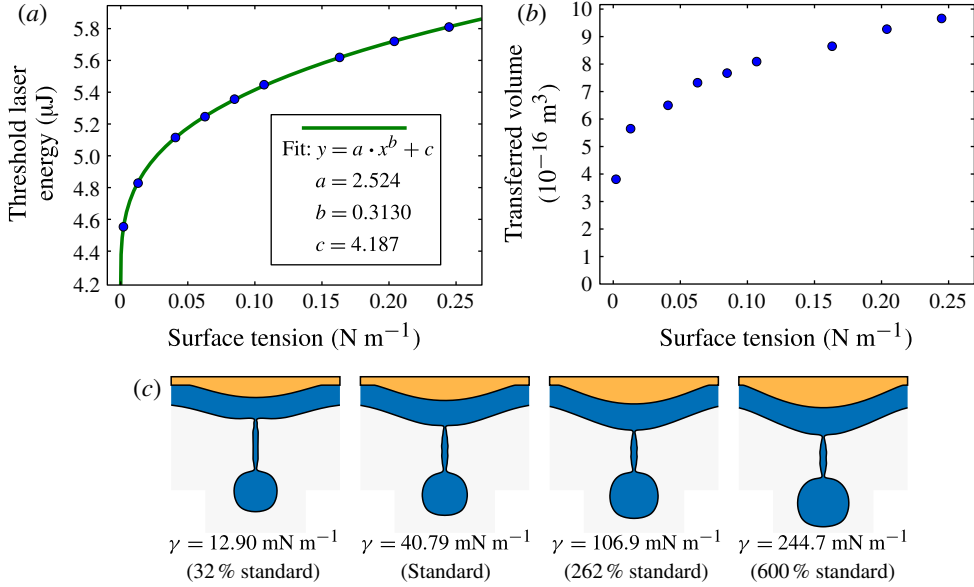


FIGURE 15. (Colour online) (a) Influence of surface tension on the laser energy input required for fluid ejection and (b) the resulting transferred ink volume. (c) Images at the instant of fluid pinch-off: 14.8, 8.5, 5.8 and 4.4 μs (from left to right).

forces and considering the role of gravity to be negligible, the evolution of the velocity field is entirely independent of density.

The influence of density occurs through its scaling of the fluid's kinetic energy and momentum, which are important to the long-time-scale behaviour of the flow when surface tension and viscosity are significant. The relative importance of viscous and surface forces are scaled by the fluid's density ρ , such that the parameters γ/ρ and the kinematic viscosity $\nu = \mu/\rho$ are the only fluid parameters needed to uniquely determine the flow behaviour. This is verified by comparing simulation results in which the surface tension, viscosity and fluid densities are jointly varied by a factor of 1000. Both the jet length and its tip velocity differ by less than 0.4 % at 2 μs .

One might object that the boundary conditions do not account for the influence of ink density on the blister expansion. However, previous experimental results (Brown *et al.* 2010) show that the blister evolution is independent of whether or not a film of NMP is present, so it is likely that over a realistic range of ink densities, the blister evolution would not be altered by a thin layer of ink.

6.2. Ink surface tension

In order to investigate the influence of surface tension, simulations are conducted using the standard set of parameters with surface tension systematically varied over the range $\gamma = 2\text{--}245 \text{ mN m}^{-1}$. For each value of surface tension, the threshold energy for transfer is determined within 3 nJ. These threshold laser energies are plotted as a function of surface tension in figure 15(a), and the corresponding transferred volumes are plotted in figure 15(b). A snapshot of the jet at the instant of pinch-off is also shown for several values of surface tension in figure 15(c).

Figure 15(a) shows that the laser energy input required for transfer increases with the surface tension, exhibiting a power-law behaviour with an exponent of 0.3130.

Likewise, the volume transferred at threshold decreases with surface tension with a trend that suggests it approaches zero as the surface tension is reduced toward zero. While the surface tensions of most fluids are of the order of tens of mN m^{-1} at room temperature, surface tension decays to zero as the critical temperature is approached. Therefore, reduction of surface tension through heating may be one avenue in which to improve the resolution of laser-induced printing.

Figure 15(c) shows that the shape of the jet at pinch-off does not significantly change as the surface tension is varied. However, this may be due in part to the fact that all of the simulations were conducted using a relatively low viscosity of $\mu = 1.7 \text{ mPa s}$. The time at which pinch-off occurs decreases from $14.8 \mu\text{s}$ at $\gamma = 2 \text{ mN m}^{-1}$ to $4.4 \mu\text{s}$ at $\gamma = 245 \text{ mN m}^{-1}$. The length of the jet at pinch-off also increases slightly with surface tension.

Insight into these dependencies involving surface tension can be gained by considering an energy balance. Conservation of the total energy (E_T) for this system can be written as

$$\Delta E_T = 0 = \Delta E_k + \Delta E_s + \Delta E_d, \quad (6.1)$$

where any reduction to the kinetic energy (E_k) is balanced by an increase in surface energy (E_s) or converted to heat through viscous dissipation (E_d). We choose $t_0 = 300 \text{ ns}$ as our initial time to evaluate the kinetic energy, for which figure 11 gives $E_k(t_0) \sim (E - E_{th})^{4.5}$. Recalling that E_{th} is the threshold energy for blister formation ($3.65 \mu\text{J}$), not pinch-off, we define $\bar{E} \equiv E - E_{th}$ as the laser energy in excess of the blister formation threshold, such that $E_k(t_0) \sim \bar{E}^{4.5}$.

Next, assuming the threshold laser energy for pinch-off has been used ($\bar{E} = \bar{E}_{th}$), we consider the energy of the system just after pinch-off for the range of γ considered in figure 15. The viscosity for this case was relatively low, so we neglect the kinetic energy loss to dissipation. Also, since the laser energy was chosen to be the threshold value, the fluid velocities near pinch-off are negligible compared with those at time t_0 (see supplementary movie 2 for the variation of velocities with time). Therefore, near pinch-off, we make the approximation that all of the initial kinetic energy is converted to surface energy ($E_s = \gamma \Delta A$ with ΔA the increase in surface area), leading to the relation that

$$E_k(t_0) \sim \bar{E}_{th}^{4.5} \sim \gamma \Delta A. \quad (6.2)$$

Inspection of figure 15(c) shows that at pinch-off, the film surface, the droplet and the thin tail behind the droplet have similar dimensions and, hence, similar surface area over the range of γ tested. Therefore, if we assume that surface area at pinch-off is relatively independent of \bar{E}_{th} , then

$$\bar{E}_{th}^{4.5} \sim \gamma. \quad (6.3)$$

Solving for \bar{E}_{th} , we get

$$\bar{E}_{th} \sim \gamma^{0.22}, \quad (6.4)$$

which suggests the plausibility of the exponent of 0.3130 obtained computationally (figure 15a). The fact that transferred volume is found to increase with γ gives ΔA some surface tension dependence, which pushes the exponent closer to 0.3130.

6.3. Ink viscosity

Simulations are also conducted using the standard set of parameters with viscosity systematically varied over the range $\mu = 0.54\text{--}54 \text{ mPa s}$. For each value of viscosity,

the threshold energy for transfer is determined within 2 nJ. These threshold laser energies are plotted as a function of viscosity in figure 16(a), and the corresponding transferred volumes are plotted in figure 16(b). A snapshot of the jet at the instant of pinch-off is also shown for several viscosities in figure 16(c).

Figure 16(a) shows that the laser energy input required for transfer increases with ink viscosity, exhibiting a linear dependence. However, the volume transferred at threshold decreases with increasing viscosity (figure 16b). This decrease can be attributed to a thinning in jet diameter with increased viscosity, resulting in similar behaviour to that discussed in § 5.2. As can be seen in figure 16(c), the jets become thinner and more elongated with increasing viscosity before pinch-off occurs.

These results can also be viewed in terms of the Ohnesorge number, $Oh = \mu / \sqrt{\rho \gamma l}$, introduced in § 1, which relates viscous forces to inertial and surface tension forces. Using the standard ink properties and a typical jet diameter of 8 μm , the Ohnesorge number is $Oh = 0.09$. The Ohnesorge number scales linearly with viscosity, and in figure 16(c), the large- Oh behaviour of long fluid threads is clearly demonstrated in the two snapshots for viscosities of 1000 and 3162 % of the standard value, corresponding to $Oh = 0.9$ and $Oh = 2.8$. In principle, one could also obtain these long threads by increasing the Ohnesorge number without increasing viscosity, for example, by decreasing ρ and γ .

The mechanism for the linear relation between threshold laser energy and viscosity is not currently understood, and the energy balance equation (6.1) does not lead to a straightforward estimate of this dependence. The first issue is that the result from figure 11(b) of $E_k(300 \text{ ns}) \sim (E - E_{th})^{4.5}$ no longer applies at large viscosities, as viscous dissipation significantly decreases the kinetic energy early on in the process. Second, in order to obtain the desired linear relationship, we need to estimate the dissipated energy in terms of viscosity and laser energy. With the significant variation over time between the short jets of low-viscosity cases and long, slender jets of high-viscosity cases, it is unlikely that a simple scaling argument can physically account for the dissipated energy, but a more complete analysis computing and integrating the dissipation from numerical data is beyond the scope of this paper. Nonetheless, this linear dependence provides valuable empirical information to help guide future experiments and optimize industrial implementations of LIFT printing.

In order to further explore the influence of viscosity, the simulation results of figure 9 are repeated using 10 times the viscosity ($\mu = 17 \text{ mPa s}$). A comparison of the transferred ink volume versus laser energy input for both viscosities is presented in Other Supplementary Material. By increasing the viscosity by a factor of 10, the range over which the transferred volume initially decreases is reduced from $\Delta E = 0.185 \text{ }\mu\text{J}$ to $\Delta E = 0.125 \text{ }\mu\text{J}$. Also, due to the greater viscous dissipation of kinetic energy, the slope of transferred volume versus laser energy decreases from $1.2 \times 10^{-9} \text{ m}^3 (\mu\text{J})^{-1}$ to $8.5 \times 10^{-10} \text{ m}^3 (\mu\text{J})^{-1}$.

6.4. Ink film thickness

The influence of donor-film thickness is also investigated by varying the initial film thickness used in the simulations between 1–10 μm . For each thickness, the transfer-threshold energy is determined to within 2 nJ. These threshold laser energies are plotted as a function of film thickness in figure 17(a), and the corresponding transferred volumes are plotted in figure 17(b). A snapshot of the jet at the instant of pinch-off is also shown for each thickness in figure 17(c).

Figure 17(a) shows that for large film thicknesses, the laser energy input required for transfer initially decreases as the film thickness is reduced; however, it reaches a

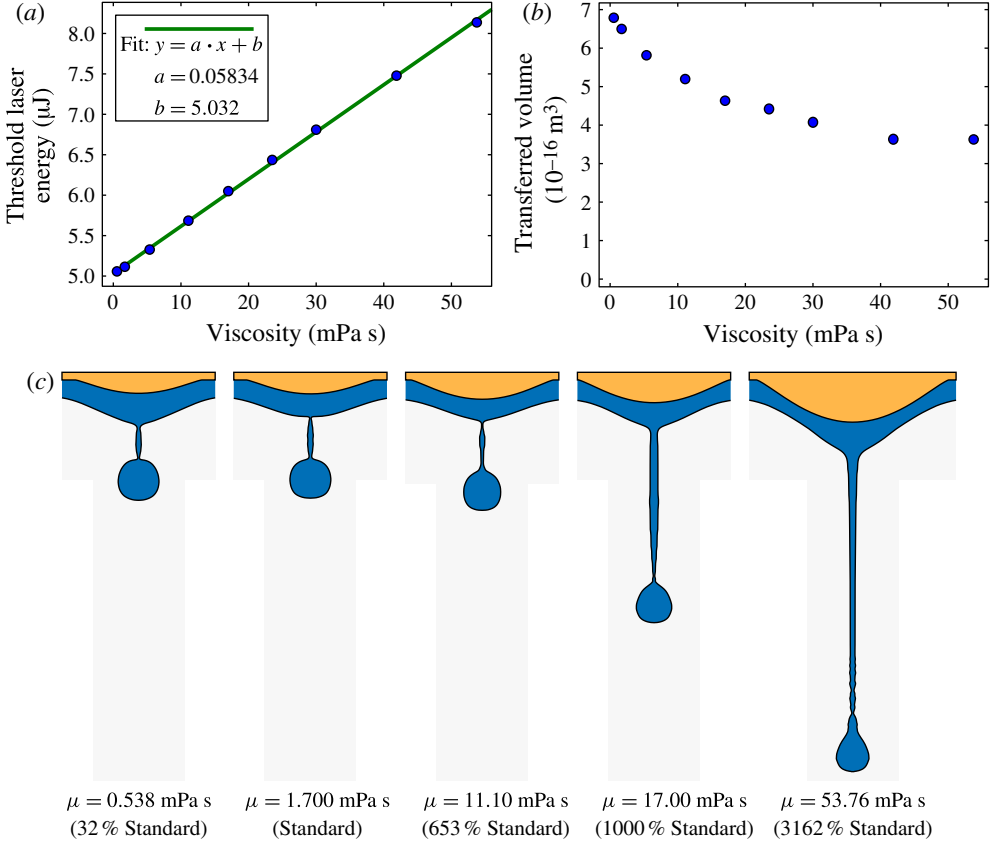


FIGURE 16. (Colour online) (a) Influence of viscosity on the laser energy input required for fluid ejection; and (b) the resulting transferred ink volume. (c) Images at the instant of fluid pinch-off: 8.6, 8.5, 11.1, 11.5 and 17.3 μs (from left to right).

minimum for a 2.5 μm film and then increases with further reduction. This transition in the scaling behaviour can be attributed to competing factors that dominate at different thickness extremes.

When the ink-film thickness is large relative to the blister width, the dependence on film thickness is dominated by the extent to which the initial impulse from the blister diverges as it is transmitted over the distance to the free surface. As discussed in §6.1, the fluid motion is initiated by a prescribed boundary displacement, which is independent of the inertial resistance provided by the ink. Therefore, the dependence on film thickness cannot be attributed to changes in the total mass of the film. Instead, reducing film thickness allows a more efficient coupling between the blister expansion and the free surface. For example, the ratio of the initial free-surface velocity (V_{f1}) to the blister expansion velocity (V_b) increases from 61 % for a 10 μm film to 76 % for a 5 μm film. With a 2.5 μm film, the two velocities are nearly equal. In addition, this more efficient coupling causes the free-surface displacement to more directly track the blister's displacement during its expansion, allowing it to impose its curved profile onto the ink-film surface. Previous work has shown that curved interfaces are more amenable to free-surface jet formation (Antkowiak *et al.* 2007).

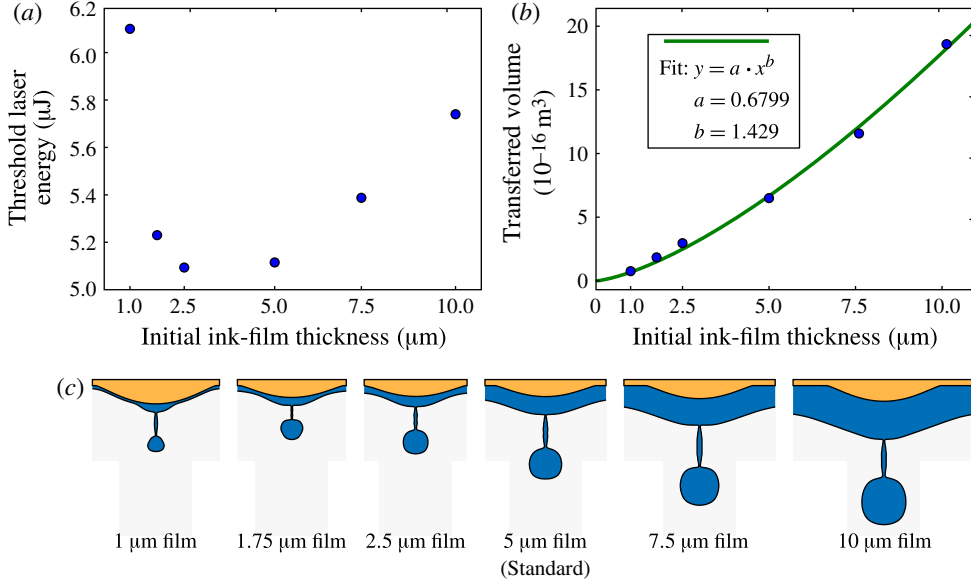


FIGURE 17. (Colour online) Simulation results for blister-actuated ejections of the standard ink ($\mu = 1.7 \text{ mPa s}$, $\rho = 1030 \text{ kg m}^{-3}$, $\gamma = 40.79 \text{ mN m}^{-1}$) using a range of initial ink-film thicknesses. (a) Laser energy required for transfer plotted as a function of film thickness; and (b) the corresponding volumes of ink transferred. (c) Images at the moment of droplet pinch-off: 3.0, 4.9, 5.7, 8.5, 11.4 and $14.0 \mu\text{s}$ for 1, 1.75, 2.5, 5, 7.5 and $10 \mu\text{m}$ films, respectively.

Reducing the film thickness results in higher initial flow velocities. However, it also enhances the influence of viscous stresses on the evolution of the flow. As the film thickness shrinks, the boundary layer spans the film thickness in less time and the energy required to shear the liquid surface a fixed distance increases. At a critical thickness, the increase in viscous resistance offsets the improvement to the coupling between the blister and free surface, resulting in a local minimum in the laser energy required for transfer. This local minimum is relevant for transferring sensitive donor materials because it minimizes the mechanical stresses placed on the ink. Below this critical thickness, viscous effects dominate, and the threshold energy increases rapidly as the film thickness is further reduced. This transition is expected to occur at larger film thicknesses as the viscosity of the ink is increased.

In contrast, the corresponding volume of fluid transferred at threshold decreases monotonically as the film thickness is reduced (figure 17b). This can be motivated by making the simple approximation that the droplet volume V_d is proportional to the volume of the disc of fluid accelerated by the blister (referred to in the kinetic energy argument in § 5.1), resulting in $V_d \sim R_0^2 H_f$. Thus, this approximation predicts a linear dependence of droplet volume on film thickness, suggesting the plausibility of the result in figure 17.

These results suggest that for applications requiring high-resolution printing, the thinnest possible films should be used. However, it is possible that the high laser energies required to transfer very thin films could result in instabilities, which limit the accuracy of droplet placement on the acceptor substrate. Also, a lower limit on ink film thickness is set by the maximum laser energy that the laser-absorbing layer

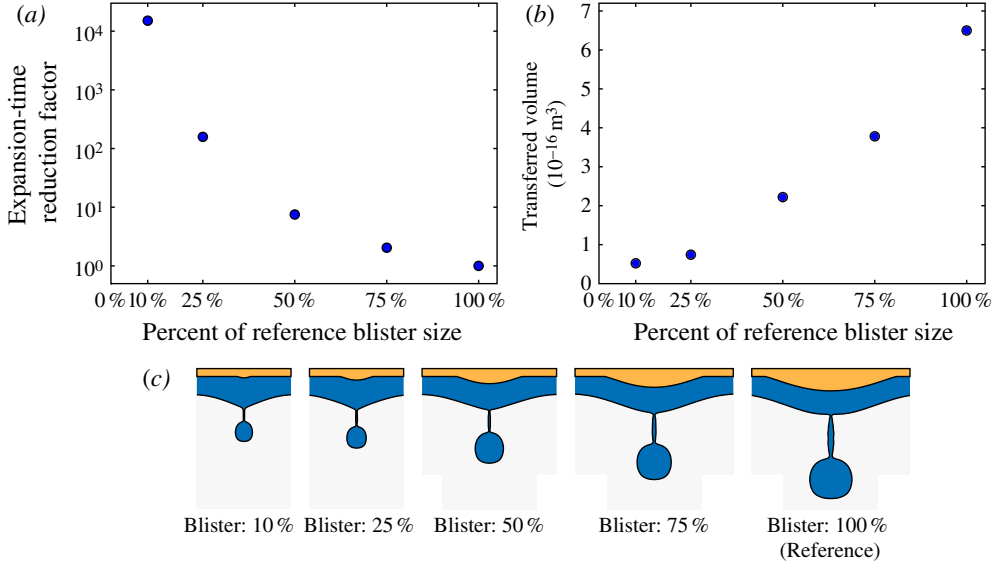


FIGURE 18. (Colour online) Simulation results for blister-actuated ejections of the standard ink using a range of blister sizes. (a) The factor by which the blister expansion time must be reduced to enable transfer is plotted against blister size. (b) The corresponding volumes of ink transferred. (c) Images at the moment of droplet pinch-off: 2.7, 3.2, 5.3, 6.5 and $8.5 \mu\text{s}$ for blisters that are 10, 25, 50, 75 and 100 % of the standard size, respectively.

can sustain without rupturing and releasing hot gases from the blister (Brown *et al.* 2010, 2011).

6.5. Blister size

In the previous sections, the effect of the laser pulse was incorporated into the simulations through the blister displacement function, which prescribes the blister's size, shape and expansion rate (equations (2.1)–(2.5)). The displacement function was developed from experimental measurements for one specific laser-absorbing layer and beam size. However, by changing the beam diameter and absorbing-layer properties, different blister responses can be achieved (Brown *et al.* 2010; Kattamis *et al.* 2011). For example, by reducing the beam size and engineering a stiffer absorbing layer to accept higher-energy laser pulses, it may be possible to produce smaller, more rapidly expanding blisters.

In this section, we investigate the potential of using smaller blisters to eject ink. The blister produced during the threshold transfer ($E = 5.115 \mu\text{J}$) of the standard ink is used as a reference. This reference blister expands to a height of $3.6 \mu\text{m}$ and a width of $33.4 \mu\text{m}$ with a temporal evolution prescribed by (2.5). Smaller blisters are created by uniformly scaling these dimensions. In order for these smaller blisters to provide a sufficient impulse for ink ejection, their temporal evolution (2.5) must also be uniformly scaled to yield a more rapid expansion. For each blister size, the factor by which the expansion time must be reduced is determined within 0.1 %. These expansion-time reduction factors are shown plotted on a logarithmic scale as a function of the blister's size in figure 18(a). The corresponding transferred volume is shown plotted in figure 18(b). Images at the moment of droplet pinch-off are also shown for each case figure 18(c).

The expansion time required for ink ejection decreases rapidly as the blister size is reduced. For example, with a blister that is half the reference size, the expansion time must be reduced by a factor of 7.5 to produce a sufficiently rapid blister expansion to eject the ink. This results in a 66% reduction in the transferred ink volume. As the blister is reduced to one-tenth size, the ejected volume drops to 8% of the reference case. This volume is equivalent to a $5.8\text{ }\mu\text{m}$ diameter hemispherical droplet (52 fl). However, in order to achieve this transfer, the expansion rate must be increased by a factor of 1.51×10^4 relative to the reference case, so that the blister reaches 95% of its final height within 0.020 ns. We note that the simple model described in the previous section would suggest that transferred volume increases with the square of blister size.

Such a rapid expansion may not be physically possible. However, based on the results from the previous section, using a thinner ink film in conjunction with the smaller blisters may allow smaller volumes with more-reasonable expansion rates. For example, if the one-tenth-size blister is instead transferring from a $1\text{ }\mu\text{m}$ donor film, the expansion rate only needs to be increased by a factor of 106, and the resulting transferred volume is equivalent to a $1.8\text{ }\mu\text{m}$ diameter hemispherical droplet (1.4 fl). Therefore, engineering the absorbing layer to enable smaller, more rapidly expanding blisters holds promise as a means to improve printing resolution during LIFT.

7. Conclusions

In summary, we have developed a computational model for the blister-actuated ejection of fluid from a thin donor film. Flow within the model is driven by a prescribed boundary displacement that matches experimental measurements of a deforming blister boundary. The accuracy of the model is first validated against experimental results. Rendered images of the simulated jets compare favourably with time-resolved images of experimentally produced jets, both in the temporal evolution and the size of the features formed. In addition, model predictions of deposited volumes of ink agree well with corresponding experimental measurements. The validated model is then used to interrogate the details of the blister-actuated flow, including velocity and pressure fields.

During early times ($t \lesssim 300\text{ ns}$), significant blister deformation occurs, and flow within the film is dominated by inertial forces. During this period, the magnitude of kinetic energy deposition is determined by the rate and extent of the blister-boundary deformation, which is controlled by the laser energy input (E). Beyond 300 ns, the blister boundary remains effectively static and no longer exchanges energy with the fluid. However, residual kinetic energy within the ink enables its continued downward flow and development into a free-surface jet. If the magnitude of this residual energy is sufficient, the jet can overcome viscous forces and surface tension and continue propagating towards the acceptor substrate, enabling ink to be deposited.

Simulation results demonstrate that the minimum energy input required for deposition and the resulting deposited volume increase with the surface tension of the ink. With an increase in ink viscosity, the laser energy required for deposition increases, but the corresponding deposited volume decreases. The influence of ink film thickness is also probed, demonstrating that droplet volume decreases with a reduction in ink film thickness, but there is an optimal film thickness at which the laser energy required for deposition is lowest. These results indicate that using a thin film of viscous ink with a low surface tension should allow the smallest volumes of deposited ink. Furthermore, simulation results using smaller blisters suggest that by engineering

a stiffer laser-absorbing layer, which produces smaller, more rapidly expanding blisters, could allow significant reductions in the deposited ink volumes.

Acknowledgements

The authors thank H. Stone, N. Kattamis and N. Hawker for valuable discussions and Dr M. Megahed and the ESI Group for allowing the use of the CFD-ACE suite. Funding for this research was provided by the Engineering and Physical Sciences Research Council through grant EP/F033710/1, the Oxford–Princeton Exchange Program, the National Science Foundation through NSF-DMR-0548147, the MRSEC program through grant NSF-DMR-0819860, and the Air Force Office of Scientific Research (AFOSR-FA9550-08-1-0094). M.S.B. was supported in part by an NSF-IGERT fellowship, grant #0903661 (Nanotechnology for Clean Energy).

Supplementary movies

Supplementary movies are available at <http://dx.doi.org/10.1017/jfm.2012.337>.

REFERENCES

- ANTKOWIAK, A., BREMOND, N., LE DIZES, S. & VILLERMAUX, E. 2007 Short-term dynamics of a density interface following an impact. *J. Fluid Mech.* **577**, 241–250.
- ARJUN, A. & WAN, K. T. 2005 Derivation of the strain energy release rate g from first principles for the pressurized blister test. *Intl J. Adhes. Adhes.* **25** (1), 13–18.
- ARNOLD, C. B., KIM, H. & PIQUÉ, A. 2004 Laser direct write of planar alkaline microbatteries. *Appl. Phys. A-Mater. Sci. Process.* **79** (3), 417–420.
- ARNOLD, C. B., SERRA, P. & PIQUÉ, A. 2007 Laser direct-write techniques for printing of complex materials. *MRS Bull.* **32** (1), 23–31.
- ARNOLD, C. B., WARTENA, R. C., SWIDER-LYONS, K. E. & PIQUÉ, A. 2003 Direct-write planar microultracapacitors by laser engineering. *J. Electrochem. Soc.* **150** (5), A571–A575.
- BARRON, J. A., WU, P., LADOUCEUR, H. D. & RINGEISEN, B. R. 2004 Biological laser printing: a novel technique for creating heterogeneous three-dimensional cell patterns. *Biomed. Microdevices* **6** (2), 139–147.
- BLAKE, J. R. & GIBSON, D. C. 1987 Cavitation bubbles near boundaries. *Annu. Rev. Fluid Mech.* **19**, 99–123.
- BOHANDY, J., KIM, B. F. & ADRIAN, F. J. 1986 Metal-deposition from a supported metal-film using an excimer laser. *J. Appl. Phys.* **60** (4), 1538–1539.
- BOUTOPOULOS, C., TSOUTI, V., GOUSTOURIDIS, D., CHATZANDROULIS, S. & ZERGIOTI, I. 2008 Liquid phase direct laser printing of polymers for chemical sensing applications. *Appl. Phys. Lett.* **93** (19), 191109.
- BROWN, M. S., KATTAMIS, N. T. & ARNOLD, C. B. 2010 Time-resolved study of polyimide absorption layers for blister-actuated laser-induced forward transfer. *J. Appl. Phys.* **107** (8), 083103.
- BROWN, M. S., KATTAMIS, N. T. & ARNOLD, C. B. 2011 Time-resolved dynamics of laser-induced micro-jets from thin liquid films. *Microfluid Nanofluid* 1–9.
- COLINA, M., DUOCASTELLA, M., FERNÁNDEZ-PRADAS, J. M., SERRA, P. & MORENZA, J. L. 2006 Laser-induced forward transfer of liquids: study of the droplet ejection process. *J. Appl. Phys.* **99** (8), 084909.
- COLINA, M., SERRA, P., FERNÁNDEZ-PRADAS, J. M., SEVILLA, L. & MORENZA, J. L. 2005 DNA deposition through laser induced forward transfer. *Biosens. Bioelectr.* **20** (8), 1638–1642.
- DINCA, V., FARSARI, M., KAFETZOPOULOS, D., POPESCU, A., DINESCU, M. & FOTAKIS, C. 2008 Patterning parameters for biomolecules microarrays constructed with nanosecond and femtosecond UV lasers. *Thin Solid Films* **516** (18), 6504–6511.

- DORAISWAMY, A., NARAYAN, R. J., LIPPERT, T., URECH, L., WOKAUN, A., NAGEL, M., HOPP, B., DINESCU, M., MODI, R., AUYEUNG, R. C. Y. & CHRISEY, D. B. 2006 Excimer laser forward transfer of mammalian cells using a novel triazene absorbing layer. *Appl. Surf. Sci.* **252** (13), 4743–4747.
- DUCHEMIN, L., POPINET, S., JOSSERAND, C. & ZALESKI, S. 2002 Jet formation in bubbles bursting at a free surface. *Phys. Fluids* **14** (9), 3000–3008.
- DUOCASTELLA, M., COLINA, M., FERNÁNDEZ-PRADAS, J. M., SERRA, P. & MORENZA, J. L. 2007 Study of the laser-induced forward transfer of liquids for laser bioprinting. *Appl. Surf. Sci.* **253** (19), 7855–7859.
- DUOCASTELLA, M., FERNÁNDEZ-PRADAS, J. M., MORENZA, J. L. & SERRA, P. 2009 Time-resolved imaging of the laser forward transfer of liquids. *J. Appl. Phys.* **106** (8), 084907.
- EGGERS, J. 1997 Nonlinear dynamics and breakup of free-surface flows. *Rev. Mod. Phys.* **69** (3), 865–929.
- EGGERS, J. & DUPONT, T. F. 1994 Drop formation in a one-dimensional approximation of the Navier–Stokes equation. *J. Fluid Mech.* **262**, 205–221.
- EGGERS, J. & VILLERMAUX, E. 2008 Physics of liquid jets. *Rep. Prog. Phys.* **71** (3), 036601.
- ESI CFD Inc. (2009) CFD-ACE+ User manual, v2009.2 edition. ESI CFD Inc., 6767 Old Madison Pike, Ste. 600, Huntsville, AL 35806, USA.
- GEKLE, S., GORDILLO, J. M., VAN DER MEER, D. & LOHSE, D. 2009 High-speed jet formation after solid object impact. *Phys. Rev. Lett.* **102** (3), 034502.
- HIRT, C. W. & NICHOLS, B. D. 1981 Volume of fluid (VOF) method for the dynamics of free boundaries. *J. Comput. Phys.* **39** (1), 201–225.
- HOPP, B., SMAUSZ, T., ANTAL, ZS, KRESZ, N., BOR, ZS & CHRISEY, D. 2004 Absorbing film assisted laser induced forward transfer of fungi (*Trichoderma conidia*). *J. Appl. Phys.* **96** (6), 3478–3481.
- HOPP, B., SMAUSZ, T., KRESZ, N., BARNÁ, N., BOR, Z., KOLOZSVARI, L., CHRISEY, D. B., SZABO, A. & NOGRADI, A. 2005 Survival and proliferative ability of various living cell types after laser-induced forward transfer. *Tissue Engng* **11** (11–12), 1817–1823.
- JOSSERAND, C., LEMOYNE, L., TROEGER, R. & ZALESKI, S. 2005 Droplet impact on a dry surface: triggering the splash with a small obstacle. *J. Fluid Mech.* **524**, 47–56.
- KATTAMIS, N. T., BROWN, M. S. & ARNOLD, C. B. 2011 Finite element analysis of blister formation in laser-induced forward transfer. *J. Mater. Res.* **26** (18), 2438–2449.
- KATTAMIS, N. T., MCDANIEL, N. D., BERNHARD, S. & ARNOLD, C. B. 2009 Laser direct write printing of sensitive and robust light emitting organic molecules. *Appl. Phys. Lett.* **94** (10), 103306.
- KATTAMIS, N. T., PURNICK, P. E., WEISS, R. & ARNOLD, C. B. 2007 Thick film laser induced forward transfer for deposition of thermally and mechanically sensitive materials. *Appl. Phys. Lett.* **91** (17), 171120.
- KIM, H., AUYEUNG, R. C. Y. & PIQUÉ, A. 2007 Laser-printed thick-film electrodes for solid-state rechargeable Li-ion microbatteries. *J. Power Sources* **165** (1), 413–419.
- KLEEFMAN, K. M. T., FEKKEN, G., VELDMAN, A. E. P., IWANOWSKI, B. & BUCHNER, B. 2005 A volume-of-fluid based simulation method for wave impact problems. *J. Comput. Phys.* **206** (1), 363–393.
- KOTHE, D. B., RIDER, W. J., MOSSO, S. J., BROCK, J. S. & HOCHSTEIN, J. I. 1996 Volume tracking of interfaces having surface tension in two and three dimensions. *AIAA Paper*, 96-0859.
- KYRKIS, A. A., ANDREADAKI, K. D., PAPAZOGLU, D. G. & ZERGIOTI, I. 2006 *Recent Advances in Laser Processing of Materials*, pp. 213–241 Elsevier, chapter 7.
- LEWIS, B. R., KINZEL, E. C., LAURENDEAU, N. M., LUCHT, R. P. & XU, X. F. 2006 Planar laser imaging and modelling of matrix-assisted pulsed-laser evaporation direct write in the bubble regime. *J. Appl. Phys.* **100** (3), 033107.
- LIN, Y. F., HUANG, Y. & CHRISEY, D. B. 2009 Droplet formation in matrix-assisted pulsed-laser evaporation direct writing of glycerol–water solution. *J. Appl. Phys.* **105** (9), 093111.

- PIQUÉ, A., CHRISEY, D. B., AUYEUNG, R. C. Y., FITZ-GERALD, J., WU, H. D., MCGILL, R. A., LAKEOU, S., WU, P. K., NGUYEN, V. & DUIGNAN, M. 1999 A novel laser transfer process for direct writing of electronic and sensor materials. *Appl. Phys. A* **69** (7), S279–S284.
- PIQUÉ, A., CHRISEY, D. B., FITZ-GERALD, J. M., MCGILL, R. A., AUYEUNG, R. C. Y., WU, H. D., LAKEOU, S., NGUYEN, V., CHUNG, R. & DUIGNAN, M. 2000 Direct writing of electronic and sensor materials using a laser transfer technique. *J. Mater. Res.* **15** (9), 1872–1875.
- PIQUÉ, A., KIM, H. & ARNOLD, C. B. 2006 *Laser Ablation and Applications*, pp. 339–373 Springer, chapter 14.
- PLATEAU, J. 1873 *Statique Expérimentale et Théorique des Liquides Soumis aux Seules Forces Moléculaires*. Gauthier-Villars.
- POPINET, S. 2009 An accurate adaptive solver for surface-tension-driven interfacial flows. *J. Comput. Phys.* **228** (16), 5838–5866.
- RAYLEIGH, LORD 1878 On the instability of jets. *Proc. Lond. Math. Soc.* **10**, 4–13.
- RIDER, W. J., KOTHE, D. B., MOSSO, S. J., CERRUTTI, J. H. & HOCHSTEIN, J. I. 1995 Accurate solution algorithms for incompressible multiphase flows. *AIAA Paper*, 95-0699.
- SERRA, P., COLINA, M., FERNÁNDEZ-PRADAS, J. M., SEVILLA, L. & MORENZA, J. L. 2004 Preparation of functional DNA microarrays through laser-induced forward transfer. *Appl. Phys. Lett.* **85** (9), 1639–1641.
- SERRA, P., FERNANDEZ-PRADAS, J. M., COLINA, M., DUOCASTELLA, M., DOMINGUEZ, J. & MORENZA, J. L. 2006 Laser-induced forward transfer: a direct-writing technique for biosensors preparation. *J. Laser Micro/Nanoeng.* **1** (3), 236–242.
- SIKALO, S., WILHELM, H. D., ROISMAN, I. V., JAKIRLIC, S. & TROPEA, C. 2005 Dynamic contact angle of spreading droplets: experiments and simulations. *Phys. Fluids* **17**, 062103.
- TENG, H., KINOSHITA, C. M. & MASUTANI, S. M. 1995 Prediction of droplet size from the breakup of cylindrical liquid jets. *Intl J. Multiphase Flow* **21** (1), 129–136.
- TJAN, K. K. & PHILLIPS, W. R. C. 2007 On impulsively generated inviscid axisymmetric surface jets, waves and drops. *J. Fluid Mech.* **576**, 377–403.
- VAN DOORMAAL, J. P. & RAITHEY, G. D. 1984 Enhancements of the simple method for predicting incompressible fluid flows. *Numer. Heat Transfer* **7** (2), 147–163.
- VAN HOEVE, W., GEKLE, S., SNOEIJER, J. H., VERSLUIS, M., BRENNER, M. P. & LOHSE, D. 2010 Breakup of diminutive Rayleigh jets. *Phys. Fluids* **22** (12), 122003.
- WARTENA, R., CURTRIGHT, A. E., ARNOLD, C. B., PIQUÉ, A. & SWIDER-LYONS, K. E. 2004 Li-ion microbatteries generated by a laser direct-write method. *J. Power Sources* **126** (1–2), 193–202.
- WEBSTER, R. 1994 An algebraic multigrid solver for Navier–Stokes problems. *Intl J. Numer. Meth. Fluids* **18**, 761–780.
- WIJSHOFF, H. 2008 Structure- and fluid-dynamics in piezo inkjet printheads. PhD thesis, University of Twente, Enschede, January.
- YOUNG, D., AUYEUNG, R. C. Y., PIQUÉ, A., CHRISEY, D. B. & DLOTT, D. D. 2002 Plume and jetting regimes in a laser based forward transfer process as observed by time-resolved optical microscopy. *Appl. Surf. Sci.* **197**, 181–187.
- ZEFF, B. W., KLEBER, B., FINEBERG, J. & LATHROP, D. P. 2000 Singularity dynamics in curvature collapse and jet eruption on a fluid surface. *Nature* **403** (6768), 401–404.